Acta Astronautica 220 (2024) 75–87

Contents lists available at ScienceDirect

Acta Astronautica

journal homepage: www.elsevier.com/locate/actaastro

# Mission analysis and guidance and control for the SpEye inspection CubeSat ☆

Giacomo Borelli [a,*], Gabriella Gaias [a], Yu Nakajima [b], Camilla Colombo [a], Vincenzo Capuano [c], Fabio Saggiomo [c], Giuseppe Leccese [d], Silvia Natalucci [d]

[a] Politecnico di Milano, 20156, Milano, Italy
[b] Japan Aerospace Exploration Agency, 2-1-1 Sengen, Tsukuba, Ibaraki, 305-8505, Japan
[c] Techno System Dev. S.r.l., Via Provinciale Pianura 2, San Martino Zona Industriale, 80078 Pozzuoli, Italy
[d] Agenzia Spaziale Italiana (ASI), Via del Politecnico snc, 00133 Roma, Italy

ARTICLE INFO

*Keywords:*
CubeSat
Proximity operations
Inspection
Flight safety

ABSTRACT

The space community is moving forward with the development of in-orbit servicing and removal technologies to enable the circular economy in space and improve future space missions' scientific and commercial return and space environment exploitation. The application of nanosatellites to carry out proximity operations presents an additional opportunity to support various novel and cost-effective distributed mission architectures. The SpEye CubeSat mission, funded by the Agenzia Spaziale Italiana in the framework of the Alcor Program, aims at demonstrating inspection and rendezvous guidance navigation and control capabilities of a nanosatellite in close-proximity of the satellite carrier in a low Earth orbit environment. This paper focuses on the design of the SpEye mission and on the guidance and control strategies to enable its technological demonstrations. Particular attention is placed on the safety aspects of trajectory design, considered of paramount importance for the robust autonomous operations of a low-cost CubeSat in proximity to another satellite.

## 1. Introduction

Advancement in In-Orbit Servicing (IOS) and Active Debris Removal (ADR) missions and technologies has been actively pursued by the global space community in the last decade. These new mission concepts will contribute in creating a sustainable space infrastructure in the future. The ability of servicing and removing assets in orbit will enable safe operations and offer advantageous commercial returns compared to traditional monolithic one-use space platforms. Several efforts have been dedicated to the development of key technologies and capabilities in the servicing/removal mission domain. Differently from the cooperative proximity operation heritage, i.e. ATV missions to the ISS, these novel architectures are introducing complex and unique challenges. For instance, the absence of cooperation and collaboration from the target being approached and captured will complicate both the mission design and its operations.

Since the late 1990s with the Orbital Express mission [1] and Engineering Test Satellite VII (ETS-VII) [2], proximity and robotic technology demonstrations have been performed in orbit. More recently, the servicing missions MEV-1 and MEV-2 by Northrop Grumman successfully rendezvous and docked with Intelsat satellites on the geostationary ring to extend their operational lifetime. In Low Earth Orbit (LEO), NASA with the OSAM-1 mission (former Restore-L) plans to rendezvous and dock to Landsat-7 to perform servicing and refuelling tasks [3]. The ClearSpace-1 mission, funded by ESA, is set to launch in 2025 a servicer to capture and deorbit debris, namely the VESPA payload adapter [4]. The Japan Aerospace and Exploration Agency (JAXA) is also moving towards the launch and demonstration of removal mission technologies through the CRD2 program [5]. Moreover, in-orbit demonstration missions such as RemoveDEBRIS [6] and Elsa-D [7] have been launched and operated in the past years to demonstrate critical technologies applicable to ADR missions.

Within this framework, proximity operations capabilities with a free-flyer nanosatellite are of interest in the technological advancement of IOS and ADR technologies. For specific tasks, such as the inspection of an in-space object, agile small satellite platforms can aid the operations of an IOS/ADR mission. Furthermore, the utilisation of low-cost and small platforms for in-orbit experiments can serve as a means to showcase the necessary capabilities and technologies required for upcoming larger more complex missions.

A number of nanosatellite missions have been either performed or studied to work in proximity operations to other objects in space. The CPOD mission, led by Tyvak Nano-Satellites Systems, performed

☆ The present paper was presented at the International Astronautical Congress 2023 in Baku, Azerbaijan. Identification number: IAC-23-C1.4.9.80008.

* Corresponding author.
*E-mail addresses:* giacomo.borelli@polimi.it (G. Borelli), gabriella.gaias@polimi.it (G. Gaias), nakajima.yu@jaxa.jp (Y. Nakajima), camilla.colombo@polimi.it (C. Colombo).

https://doi.org/10.1016/j.actaastro.2024.04.025
Received 10 January 2024; Received in revised form 5 March 2024; Accepted 13 April 2024
Available online 16 April 2024

several proximity operations with two 3U CubeSats in LEO [8]. The Seeker mission – launched in 2019 – performed inspection manoeuvres of Cygnus after the deployment from the latter [9]. The e.inspector mission, originally studied in the concurrent design facility in ESA [10] was planned to inspect the ENVISAT failed satellite prior to a dedicated mission for its removal. At present, such a mission is developing towards the inspection of the VESPA upper stage to pave the way to the ClearSpace-1 mission [11]. The two nanosatellites of the Canadian Advanced Nanospace Experiment-4 & 5 (CanX-4 & 5) funded by the Canadian Space Agency demonstrated various formation flying and proximity operations in LEO exploiting differential GNSS relative navigation techniques.

The Space Eye (SpEye) mission is an in-orbit demonstration (IOD) mission funded by the Agenzia Spaziale Italiana (ASI) in the framework of the Alcor program. The aim of the mission is to demonstrate proximity operations technologies and capabilities in LEO by means of a 6U CubeSat flying in proximity of the ION CubeSat satellite carrier. This paper provides an overview of the mission operations design and the guidance and control strategies developed within this project. Special attention is here dedicated to the design of relative trajectories to ensure operational safety, a factor that is regarded as of utmost importance for the success of the mission. Among the several proximity guidance and control methods and approaches employed throughout the SpEye mission, this paper focuses on detailing the inspection motion planning and the close-range rendezvous guidance design.

The primary objective of the SpEye mission is to perform the inspection of the CubeSat satellite carrier. Several strategies have been developed in literature for performing the task of inspection of an in-space object. The trajectory design often depend on the specific applications, i.e. whether the target is cooperative or collaborative. Fly-around spiral trajectories are usually exploited to obtain reliable images from multiple line-of-sights, and in the case of uncooperative targets, the property of safety is enhanced. In the e.inspector ESA studies [10,11], the spiral-shape fly-arounds are employed, which exploit relative motion natural dynamics and implement the concept of E/I separation to guarantee passive abort safety of the trajectory [12]. These peculiar relative motion regimes to inspect uncooperative targets with E/I separation have been studied also in the references [3,5,13]. Of interest in inspection motion planning is the design of trajectories to fly while observing the target features in an optimal fashion. Capolupo and Labourdette [14] developed a sampling-based motion planning algorithm to design the inspection arcs around the target object considering a metric score based on the illumination conditions, safety conditions and observation completion. The work of Maestrini and Di Lizia [15] extended the latter approach considering the inspection of an object with unknown properties. Additionally, reinforcement learning strategies have also been explored as guidance and control methods to inspect in-orbit object in the reference [16]. Nakka et al. [17] developed an inspection approach that exploits an information gain metric optimisation, based on the quality of the observations obtained on stable relative orbits. In this work the latter approach is exploited and adapted to meet the peculiar conditions of the SpEye CubeSat mission. Specifically, the inspection trajectories are sampled in the relative orbital elements space, considering a constraint on the sampling arising from passive abort safety conditions. Moreover, the evaluation of feasible trajectories encompasses both energy-matching orbits and general drifting ellipses.

Furthermore, this paper details the design of the close-range rendezvous, planned during the SpEye mission as an advanced mission objective to showcase the capability of a nanosatellite to approach a target within a few meters of minimum distance. Several methods have been studied in literature, such as optimisation based methods [18–22], artificial potential functions [23,24], sampling-based methods [25] and analytic approaches [26,27]. Among this framework, optimisation methods are extremely useful in design the trajectories which minimise a cost while satisfying operational constraints, such as keep out zones or approach corridors. Of great interest in the trajectory optimisation methods applied to the proximity scenarios are the convex formulations of the guidance problem. These approaches provide a computationally efficient and robust strategy, which are extremely suitable for the high autonomy requirements involved in proximity operations [28–30]. The approach selected for this mission includes the method of Borelli et al. [31], which exploits a Sequential Convex Programming (SCP) method to generate delta-v optimal forced motion trajectories, while including advanced and stringent safety path constraints.

The paper is organised as follows: after this introduction, the description of the mission and the concept of operations with the planned in-orbit experiments and technological demonstrations is described. Subsequently, in Section 3 a concise introduction to the Relative Orbital Elements (ROE) framework used for proximity operations mission and guidance and control design is presented. Section 4 outlines the passive abort safety concept used during the proximity operations design of the SpEye mission. The description of the guidance and control strategies of the inspection phases and close-range rendezvous phases of the mission are detailed in Sections 5 and 6 respectively. Then the conclusions and future development plans are described.

## 2. Mission description

SpEye is an in-orbit demonstration mission of various proximity operations capabilities of a nanosatellite in the servicing and removal mission framework. The in-orbit experiments will involve a free-flyer (SpEye) and a CubeSat satellite carrier. The CubeSat carrier exploited is the InOrbitNow (ION) platform of D-Orbit S.p.a. [32]. The mission is proposed and studied by a consortium of Italian entities composed of TSD Space (prime), D-Orbit, T4i, Planetek, Politecnico di Milano and Università di Napoli Federico II; and is funded within the Alcor program by the Agenzia Spaziale Italiana (ASI). The main high-level objectives of the SpEye mission are reported in Table 1 and include inspection and rendezvous operations. A series of experiments are planned for the two-satellite formation in the timeline of the mission, which aim to highlight a diverse array of operations, ranging from cooperative and collaborative scenarios to fully uncooperative and non-collaborative ones. Therefore, the SpEye mission serves as a cost-effective test bed to showcase capabilities pertinent IOS and ADR domain. Additionally, it seeks to demonstrate the effectiveness of a small and agile free-flyer in proximity operations.

The free-flyer platform is a 6U CubeSat that will be equipped with a GNSS receiver, a star tracker and additional attitude sensors, as well as an electro-optical (EO) subsystem comprising a visible camera, an infrared camera and a laser range finder. A six Degrees of Freedom (DOF) cold-gas propulsion system will be embarked to enable agile and precise control in proximity operations. Moreover, the formation will exploit an Inter-Satellite Link (ISL) active during the nominal operations to allow communication between the free-flyer and ION. Regarding absolute orbit and attitude determination, the free flyer will use a navigation filter that fuses GNSS, Star sensor, Magnetometer and Sun sensor observations with inertial measurements and with a model of the absolute translational and rotational dynamics. A sensor fusion architecture similar to the one proposed in [33,34] will be adopted. Relative navigation within a cooperative framework will leverage the processing of differential GNSS observations, achieved through the combination of code-phase and carrier-phase measurements gathered on both the free flyer and the ION carrier. The EO subsystem offers versatility by enabling pure EO-based navigation [35,36] as well as GNSS-EO-based navigation [37,38], enabling support for uncooperative proximity operations and cooperative navigation in challenging GNSS conditions, respectively.

**Table 1**
Primary high-level objectives of the SpEye mission.

| | |
|---|---|
| **Objective 1** | Demonstrate CubeSat-Carrier formation flying capabilities |
| **Objective 2** | Demonstrate autonomous inspection capabilities of the CubeSat |
| **Objective 3** | Validate mid- and close-range rendezvous capabilities of the free-flyer |

### 2.1. Concept of operations

The SpEye mission will begin on the operational orbit in LEO where the free-flyer will be released from the ION carrier. The operational orbit is selected as a near-circular Sun Synchronous Orbit (SSO) with an altitude of 535 km and a nominal Local Time of Ascending Node (LTAN) of 00:00. The choice of orbital altitude has been made following an assessment of the uncontrolled reentry duration for the nanosatellite, compliant with the space debris mitigation guidelines that requires a reentry time below 25 years from the satellite's end-of-life [39]. The nominal LTAN of the SSO is selected to ease the conditions of illuminations during proximity operations. The free-flyer is released from the ION carrier with the strategy detailed in [40], where the release mechanism equivalent delta-v is compensated with an ION correction manoeuvre to reach a safe formation configuration. The design of the release involves selecting the direction of the release in RTN and the necessary correction manoeuvre. The direction of the release is selected accounting for the expected differential drag drift to prevent any subsequent decrease of the along-track inter-satellite distance in case of an anomaly. The stable safe orbit targeted after the correction manoeuvre must maintain a separation of at least 15 km from the ION carrier to ensure ground segment trackability. Additionally, this relative orbit geometry shall be based on the E/I separation concept to ensure passive safety of the formation. After the deployment, ION will execute coarse formation keeping by means of impulsive manoeuvres to allow the necessary boot and commissioning of the SpEye free-flyer platform without letting the relative safe formation vanish. Subsequently, the far-range approach will be performed using the guidance and control strategies developed in [13,41]. Once again in this phase, ION impulsive manoeuvres will be exploited to control the formation and secure delta-v saving of the SpEye free-flyer platform. After reaching the Close Relative Parking Orbit (CPRO) condition at around 300 m of mean along track inter-satellite distance, the SpEye free-flyer overtakes the formation control and maintenance tasks. From the CPRO, three separate mission gates, composed of further proximity operations experiments, will be performed in a chronological order of increasing complexity. The three gates of the mission are described as follows:

- **Gate I — Collaborative inspection**: here the demonstrations focus on performing inspection of the ION satellite by jointly controlling both the target and the free-flyer. Capabilities related to this gate are applicable to servicing scenarios with active and collaborative platforms. This gate represents the minimum success criteria of the SpEye mission.
- **Gate II- Non-Collaborative inspection**: here the inspection operations with the free-flyer are demonstrated relying solely on the latter platform control and motion planning. The demonstrated capabilities of this gate are useful for applications to servicing/removal missions to non-active and/or uncontrolled satellites. This gate represents the full success criteria of the SpEye mission.
- **Gate III- Close-range rendezvous**: here the capabilities of the free flyer to rendezvous with a target in space are demonstrated. This gate represents the extended success criteria of the SpEye mission.

**Table 2**
SpEye mission gate planned demonstrations.

| | **Gate I** | |
|---|---|---|
| | **Conditions** | **Rel. Nav.** |
| *Demo 1.1* | Rotational collaboration of ION for inspection | DGNSS |
| | **Gate II** | |
| | **Conditions** | **Rel. Nav.** |
| *Demo 2.1* | ION stable in RTN frame | DGNSS |
| *Demo 2.2* | ION rotating with a flat spin | DGNSS+EO |
| *Demo 2.3* | ION rotating with perturbed spin | EO-only |
| | **Gate III** | |
| | **Conditions** | **Rel. Nav.** |
| *Demo 3.1* | Rendezvous to stable hold-point in RTN frame at 10 m from ION | EO assisted DGNSS |
| *Demo 3.2* | Rendezvous to stable hold-point in inertial frame at 10 m from ION | EO only |
| *Demo 3.3* | Rendezvous to rotating hold-point around ION at 10 m and 1 deg/s | EO only |

The experiments/demonstrations planned for each gate of the SpEye mission are reported in Table 2, together with the scenario conditions and, particularly, the relative navigation mode used. The DGNSS navigation for cooperative navigation relies on GNSS measurements solely, obtained from both the free flyer and carrier. In the EO-only navigation mode, the EO subsystem, comprising a camera suite and the LRF, supports uncooperative navigation. The DGNSS+EO mode and EO Assisted GNSS mode integrate DGNSS and EO observations with loose and tight integration, respectively, enhancing robust cooperative navigation.

Fig. 1 shows the nominal timeline of the SpEye mission, with the associated nominal operations time for each phase. Note that the allocated time is defined considering the nominal operations planned during the SpEye mission.

## 3. Relative motion preliminaries: relative orbital elements

The relative motion of two objects in orbit can be described with the quasi non-singular Relative Orbital Elements (ROEs) defined in function of the Keplerian elements of the chaser and target satellite as follows:

$$\delta\boldsymbol{\alpha} = \begin{pmatrix} \delta a \\ \delta\lambda \\ \delta e_x \\ \delta e_y \\ \delta i_x \\ \delta i_y \end{pmatrix} = \begin{pmatrix} (a_c - a_t)/a_t \\ u_c - u_t + (\Omega_c - \Omega_t)\sin i_t \\ e_c \cos\omega_c - e_t \cos\omega_t \\ e_c \sin\omega_c - e_t \sin\omega_t \\ i_c - i_t \\ (\Omega_c - \Omega_t)\sin i_t \end{pmatrix} \tag{1}$$

where $a$ is the semi-major axis, $e$ is the eccentricity, $i$ the inclination, $\Omega$ the right ascension of the ascending node, $\omega$ is the argument of pericenter and $u$ is the mean argument of latitude (defined as $u = M + \omega$). The subscript $t$ and $c$ refer to the target and chaser satellite orbit respectively. The first two components of the ROE state are the relative semi-major axis and the relative mean longitude. The other terms describe the x and y components of the relative eccentricity and relative inclination vectors, which can be also written in terms of their respective magnitude and phase:

$$\delta\boldsymbol{e} = \delta e \begin{pmatrix} \cos\varphi \\ \sin\varphi \end{pmatrix}, \quad \delta\boldsymbol{i} = \delta i \begin{pmatrix} \cos\theta \\ \sin\theta \end{pmatrix} \tag{2}$$

The $x$ and $y$ components of the vectors

In the near-circular orbit case, the unperturbed relative motion dynamics can be expressed by linearised equations and ROEs quantities

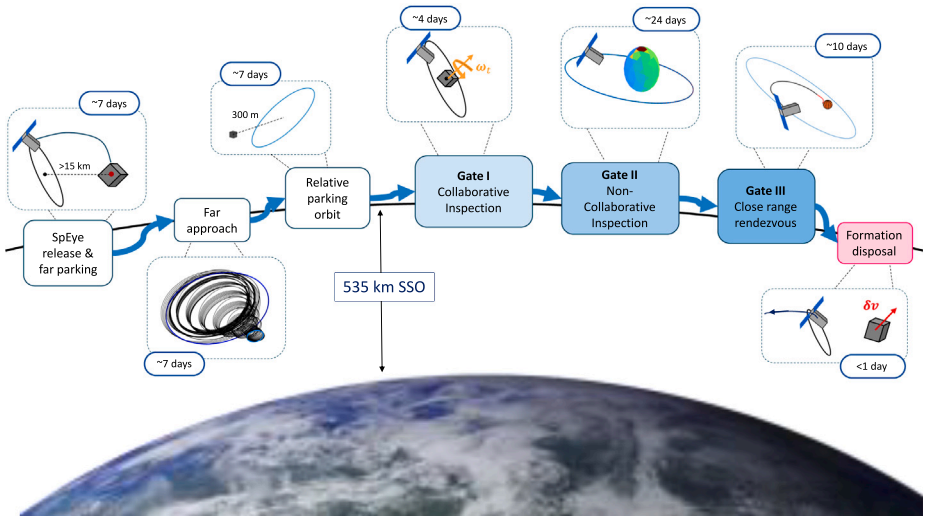


**Fig. 1.** Concept of operations of the SpEye demonstration mission.

can be associated to integrals of motion of the Clohessy–Wiltshire equations [42]. The relative dynamics written in function of the quasi-non singular ROEs is formulated as follows:

$$a\delta\dot{\boldsymbol{\alpha}} = \mathrm{A}a\delta\boldsymbol{\alpha} + \mathrm{B}\boldsymbol{f}_u \tag{3}$$

with

$$\mathrm{A} = \begin{bmatrix} 0 & 0 & 0 & 0 & 0 & 0 \\ -\frac{3}{2}n & 0 & 0 & 0 & 0 & 0 \\ 0 & 0 & 0 & 0 & 0 & 0 \\ 0 & 0 & 0 & 0 & 0 & 0 \\ 0 & 0 & 0 & 0 & 0 & 0 \\ 0 & 0 & 0 & 0 & 0 & 0 \end{bmatrix}$$

$$\mathrm{B} = \frac{1}{n}\begin{bmatrix} 0 & 2 & 0 \\ -2 & 0 & 0 \\ \sin u & 2\cos u & 0 \\ -\cos u & 2\sin u & 0 \\ 0 & 0 & \cos u \\ 0 & 0 & \sin u \end{bmatrix}$$

where A is the plant matrix, B is the control input matrix and $\boldsymbol{f}_c$ the control input. The term $n$ refers to the mean motion of the target's orbit. Note that the ROE state is multiplied by the target semi-major axis, here referred simply as $a$, to retain the desired dimensionality of the ROE components.

The unforced relative motion solution can be obtained through the State Transition Matrix (STM) as follows:

$$a\delta\boldsymbol{\alpha}(t) = \boldsymbol{\Phi}(t_0, t)a\delta\boldsymbol{\alpha}_0 \tag{4}$$

$$\boldsymbol{\Phi}(t_0, t) = \boldsymbol{\Phi}_{0,t} = \begin{bmatrix} 1 & 0 & 0 & 0 & 0 & 0 \\ -\frac{3}{2}n(t-t_0) & 1 & 0 & 0 & 0 & 0 \\ 0 & 0 & 1 & 0 & 0 & 0 \\ 0 & 0 & 0 & 1 & 0 & 0 \\ 0 & 0 & 0 & 0 & 1 & 0 \\ 0 & 0 & 0 & 0 & 0 & 1 \end{bmatrix} \tag{5}$$

The change of variable (Lyapunov transformation) between the ROE state and the Cartesian states of the Hill Clohessy–Wiltshire equations is defined as [43]:

$$\delta\boldsymbol{x} = \mathrm{T}(t)a\delta\boldsymbol{\alpha} \quad , \quad a\delta\boldsymbol{\alpha} = \mathrm{T}^{-1}(t)\delta\boldsymbol{x} \tag{6}$$

with

$$\mathrm{T}(t) = \begin{bmatrix} 1 & 0 & -\cos(nt) & -\sin(nt) & 0 & 0 \\ 0 & 1 & 2\sin(nt) & -2\cos(nt) & 0 & 0 \\ 0 & 0 & 0 & 0 & \sin(nt) & \cos(nt) \\ 0 & 0 & n\sin(nt) & -n\cos(nt) & 0 & 0 \\ -(3n)/2 & 0 & 2n\cos(nt) & 2n\sin(nt) & 0 & 0 \\ 0 & 0 & 0 & 0 & n\cos(nt) & n\sin(nt) \end{bmatrix}$$

where $\delta\boldsymbol{x}$ is the Cartesian state composed by position and velocity and velocity vector in the Radial Tangential Normal (RTN) reference frame.

Within the quasi-non singular ROE framework, the average effect of the Earth Oblateness perturbation and atmospheric drag can be readily introduced in a linear fashion with their respective state transition matrices [41,44]. Specifically, the $J_2$ perturbation is included the relative effect of the secular perturbing term, hence impacting the mean – i.e., one-orbit averaged – motion:

$$\boldsymbol{\Phi}_{kep+J_2}(t_0, t) = \begin{bmatrix} 1 & 0 & 0 & 0 & 0 & 0 \\ (\nu+\mu_A)dt & 1 & 0 & 0 & (\mu_I)dt & 0 \\ 0 & 0 & \cos(\dot{\phi}dt) & -\sin(\dot{\phi}dt) & 0 & 0 \\ 0 & 0 & \sin(\dot{\phi}dt) & \cos(\dot{\phi}dt) & 0 & 0 \\ 0 & 0 & 0 & 0 & 1 & 0 \\ \lambda_A dt & 0 & 0 & 0 & \lambda_I dt & 1 \end{bmatrix}$$

The coefficients introduced depend on the $J_2$ effects and chief orbit parameters, for more detail the reader is referred to the papers from Gaias et al. [41,44].

In the LEO environment, the atmospheric drag represents a relevant effect to account in the modelling and design. Also in relative motion, the different satellite ballistic coefficients in the formation cause a differential acceleration. Linear models and derivation of STMs including the effects of the differential drag are studied in [44,45]. The model adopted is the one introduced in Gaias et al. [44] which catches the mean effects produced by the differential drag acceleration by using a general empirical formulation (with sinusoidal form) derived from the analysis of the dynamical properties of the linearised equations of motion of near-circular orbits. The model exploits the constant quantities $a\dot{\delta a}$, $a\delta\dot{e}_x$ and $a\delta\dot{e}_y$ to represent the effects on the time variation of the relative semi-major axis and relative eccentricity vector induced by differential drag. By augmenting the ROE states of Eq. (1) with the time derivative quantities, the linear STM model for differential drag is written as follows:

$$\begin{pmatrix} a\delta\boldsymbol{\alpha}(t) \\ a\dot{\delta a}(t) \\ a\delta\dot{e}_x(t) \\ a\delta\dot{e}_y(t) \end{pmatrix} = \begin{bmatrix} \boldsymbol{\Phi}_{kep+J_2}(t_0, t) & \boldsymbol{\Phi}_{dd}(t_0, t) \\ 0_{3\times6} & 0_{3\times3} \end{bmatrix} \begin{pmatrix} a\delta\boldsymbol{\alpha}_0 \\ a\dot{\delta a}_0 \\ a\delta\dot{e}_{x0} \\ a\delta\dot{e}_{y0} \end{pmatrix} \tag{7}$$

**Table 3**
SpEye free-flyer and ION satellite carrier characteristics for the differential drag study.

| | |
|---|---|
| ION mass range | [195–230] kg |
| SpEye mass range | [11–12.1] kg |
| ION $C_d$ | 2.1 (mean) 0.2 (std) |
| SpEye $C_d$ | 2.1 (mean) 0.2 (std) |
| SpEye rotating $A_{cross}$ | 0.140 m$^2$ |
| ION rotating $A_{cross}$ | 1.977 m$^2$ |
| SpEye stable $A_{cross}$ | 0.115 m$^2$ |
| ION stable $A_{cross}$ | 1.482 m$^2$ |

where details on the expression of $\Phi_{dd}(t_0, t)$ can be found in the Ref. [44]. The effects of differential drag reflect on the ROE states as an increase of the relative semi-major axis and a movement of the relative eccentricity vector according to their time derivative values. The $a\dot{\delta}a$ is the dominating mean effect over one period, with one order of magnitude greater than the $a\dot{\delta}\boldsymbol{e}$. From an operational point of view, the $a\dot{\delta}\boldsymbol{\alpha}$ quantities are estimated onboard and continuously monitored and updated, avoiding the complex modelling of the drag coefficient, cross-sectional areas variations, and atmosphere model uncertainties in the system.

Due to its relatively low altitude in LEO, the differential drag effects experienced by the formation during the SpEye mission are significant and cannot be neglected at the preliminary design phase. A detailed analysis and characterisation of these perturbative effects was performed considering platforms parameters reported in Table 3.

The platforms mass ranges are considered to comprise values envisioned from initial to final operations along the whole mission lifetime. The rotating average area-to-mass ratio are computed with an in-house tool developed by Politecnico di Milano which models the distribution of the cross-sectional area along the motion direction considering the spacecraft shape and the available attitude orientations during operations. A detailed analysis was performed to generate the envelope of differential drag perturbative effects accounting for all the mission scenarios envisioned. The distributions of the $a\dot{\delta}\boldsymbol{\alpha}$ quantities are computed from the uncertainties of the parameters considered and detailed in Table 3. Two uniform mass distributions between the lower and upper limits for the platforms are considered, while the average cross-sectional areas is evaluated constant over one period depending on the attitude mode of the platforms. The satellites drag coefficients are evaluated with a Gaussian distribution.

Fig. 2 shows an example of the $a\dot{\delta}a$ distribution for the formation in the scenario characterised by SpEye with rotating attitude motion and ION with a stable attitude. Three cases are shown representing the low, medium and high solar activity conditions using the NRMLSISE-00 atmosphere model [46]. The low, medium an high solar activities cases refer to the conditions with exospheric temperature $T_\infty$ of respectively 750 K, 1000 K, and 1250 K. It can be noted from the Fig. 2 how the differential drag effects cause a time derivative of the relative semi-major axis with a mean value in the order of meters per period. This will cause an increase of the drift between the two satellites in the along track direction. The formation keeping strategy and manoeuvres must be planned to maintain the satellites in close formation in the desired configuration, compensating for these differential drag effects.

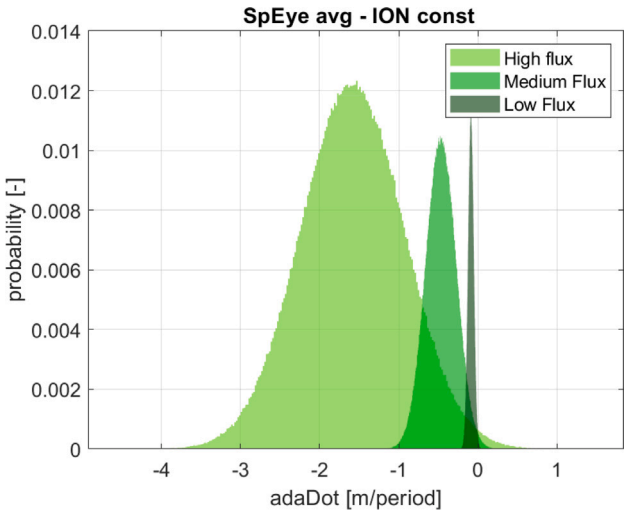


**Fig. 2.** Distribution of the $a\dot{\delta}a$ (adaDot) quantities for the conditions of Table 3 with low, medium and high solar flux in the case of ION stable and SpEye free-flyer with a rotating attitude.

## 4. Passive safety in relative motion

Flight safety represents a crucial factor in the design of the SpEye mission proximity operations. Safety is here intended as collision avoidance between the satellites involved in the formation, to guarantee the completion of all demonstrations and operations. A specific concept of safety is applied in this mission and operations design, namely the passive abort safety. This concept introduces a high level of collision avoidance robustness even in the extreme cases of major failures and complete loss of one/more satellites in the formation. A relative trajectory between a chaser and a target is defined as passively safe at time $t_i$ for a time interval of $\Delta T$ if it is outside a Keep Out Zone (KOZ) defined around the target at time $t_i$, and it will remain outside the KOZ also after a $\Delta T$ time interval of uncontrolled flight starting at $t_i$. This ensures collision avoidance over the time interval $\Delta T$ without requiring any control action, making the trajectory robust against significant malfunctions or complete loss of control capability of the chaser platform. A methodology that has been widely used in satellite proximity operations to impose a passive abort safety measure is the exploitation of the geometrical properties of the relative eccentricity and inclination vectors in a concept known as E/I separation, where E and I stand for eccentricity and inclination respectively. Specifically, the E/I separation concept has been successfully demonstrated in-flight in proximity missions. Examples are the swap of satellites in GRACE [12], the missions Tandem-X and TerraSAR-X [47], the PRISMA demonstrations mission [48], and the AVANTI experiment [41]. The E/I separation concept exploits the relative motion dynamics of objects flying on Keplerian orbits and their geometrical properties. For almost bounded relative trajectories, E/I separation relies on the (anti-)parallelism of the relative eccentricity and relative inclination vectors, see Eq. (2), to maintain a one-orbit minimum distance in the Radial and Normal (RN) plane. The minimum distance in said plane, thanks to the uncontrolled dynamics evolution of the relative trajectory on Keplerian orbits, will guarantee a minimum separation between the objects in the formation also at future times. Furthermore, the evolution of uncertainties and trajectories dispersion in relative motion will primarily be concentrated on the along-track direction, which makes even more robust the definition of minimum separation in the RN plane as passive abort safety check.

This concept of ensuring collision avoidance by imposing a minimum one-orbit distance in the RN plane is employed in the SpEye mission design. A safety tool is developed considering the method developed in Gaias and Ardaens [49], where the passive abort safety feature of a trajectory is checked considering a metric which depends on the propagation of the relative trajectory along with its uncertainties.

The minimum one-orbit distance in the RN plane $\delta r_{RN}^{min}$ is defined at each instant with the following minimisation problem in function of ROEs, according to the definitions in Eqs. (1) and (6):

$$\delta r_{RN}^{min} = \min_u \sqrt{(a\delta a - a\delta e\cos(u-\varphi))^2 + (a\delta i \sin(u-\theta))^2} \tag{8}$$

where $u$ is the mean argument of latitude on the absolute reference orbit. This geometrical problem reduces to finding the minimum distance

between the target and the relative motion ellipse in the RN plane. In the general case, the minimum distance between an ellipse and a point corresponds to one of the solution of a quartic equation [49]. Degenerate cases of the general solution are identified for example in the energy matching conditions $a\delta a = 0$, where the minimum distance can be expressed as the minor-axis of the ellipse in RN, $b_{RN}$. Furthermore, in the particular case of $a\delta a = 0$ and $\varphi = \theta$ (E/I separation) the problem reduces to the E/I separation condition, where the minimum one-orbit distance relates to the minimum between the magnitude of the relative eccentricity and relative inclination vector. In this work the minimum one-orbit distance in the RN plane is evaluated considering the solution of the quartic equation representing the distance between the target and the RN ellipse.

The criteria used as a passive abort safety check for a $\Delta T$ is defined as follows [49]:

$$\delta\bar{r}_{RN}^{min} - 3\sigma_{\delta r_{RN}^{min}} > C_{coll} \tag{9}$$

where $\delta\bar{r}_{RN}^{min}$ and $\sigma_{\delta r_{RN}^{min}}$ represent respectively the expected value and the standard deviation of the minimum one-orbit RN distance distribution. Eq. (9) is then evaluated for the time interval $\Delta T$ when passive abort safety is required. In order to compute the safety conditions in successive time instants, the state and covariance of the state (i.e., knowledge error associated to the ROE state) are propagated following the linear dynamics model described in Section 3 and reported in the following.

$$\begin{cases} a\delta\boldsymbol{\alpha}(t) = \boldsymbol{\Phi}_{0,t} a\delta\boldsymbol{\alpha}_0 \\ P(t) = \boldsymbol{\Phi}_{0,t} P_0 \boldsymbol{\Phi}_{0,t}^T \end{cases} \tag{10}$$

The minimum one-orbit distance in RN is a nonlinear expression of the current ROE state. Hence, to compute in an accurate fashion the expected value and second-order moment of its distribution, the unscented transformation is employed as in Ref. [49]. According to the number of variables influencing the minimum RN distance function, 11 sigma points are used in the unscented transformation.

In this manner, the passive abort safety check described in Eq. (9) becomes entirely analytic, requiring only linear state and covariance propagations, along with an analytic solution of a quartic equation. This facilitate a straightforward implementation in spacecraft autonomous onboard safety logics and efficient preliminary analyses.

An example of this concept is applied to generate the state space of safe trajectories in proximity for the SpEye mission. Here, passive abort safety is imposed for $\Delta T = 12$ h and considering initial errors on position and velocity as 20 cm and 5 mm/s ($1\sigma$) respectively. The differential drag perturbation is also taken into account in this example considering the condition of SpEye free-flyer with rotating attitude and ION with stable attitude and high solar activity. This corresponds to a mean $a\delta a = -1.57$ m/period. A high knowledge uncertainty on the differential drag perturbation is accounted for, including a 50% standard deviation to the nominal value. The collision margin is considered as a spherical KOZ of 4 m of radius around the carrier platform, given its physical dimension. The distributions of safe conditions in the ROE space are shown in the maps of Fig. 3, where the black dots display a safe relative orbit according to the aforementioned settings and collision check expressed in Eq. (9). The ROE conditions displayed are obtained considering a uniform sampling of the ROE states within the applicable limits. The limits considered are $|a\delta a| < 5$ m, $a\delta e < 100$ m, $a\delta i < 100$ m. Of course trajectories that exceed the upper limits in relative eccentricity and inclination vectors magnitudes will result in larger relative orbits than the state space considered, thus also satisfying naturally the passive abort safety check.

## 5. Gate II: Non-collaborative inspection design

In Gate II the goal of the SpEye mission is to demonstrate the capability of the free-flyer of performing non-collaborative inspection of the ION carrier. Here, relative inspection orbits are designed to obtain observations (i.e., images) of the ION carrier's features. As outlined in Section 2, this gate encompasses three distinct demonstrations, which differ mainly in the rotational motion of the ION satellite to emulate different scenarios of non-collaborative targets and in the navigation mode employed.

The trajectory design and motion planning during inspection are performed considering the optimisation of the information cost, a metric to quantify the quality and usefulness of a particular image of certain features of the carrier. The method is described in the subsequent sub-sections, together with the simulation results obtained for demo 2.1, where the target has a stable attitude in RTN.

### 5.1. Information cost definition

The motion planning outlined in this paper relies on a metric called information cost. This metric quantifies the quality of the observations acquired along a given trajectory. Specifically, the scalar quantity it assesses the performance of the free-flyer to comprehensively and accurately map the features of the target to be inspected. This information cost metric is based on previous developments in the literature [17,50].

The model considers a number of Points of Interest (POIs) defined on the target body, in this specific case the ION satellite carrier. Then the quality of an observation of a single point of interest $\boldsymbol{d}_{POI,j}$ from a single point of view $\boldsymbol{r}_i$ is measured as the capability of reducing the current variance of the knowledge of the POI referred as $\sigma_{0,j}$. Considering this computation for all the observation points $\boldsymbol{r}_i$ of the inspection motion planning and of the defined POIs the information cost is expressed as:

$$IC_{POI,j}(\boldsymbol{r}) = \left[\sigma_{0,j}^{-1} + \sum_{\boldsymbol{r}_i} \sigma(\boldsymbol{r}_i, \boldsymbol{d}_{POI,j})^{-1}\right]^{-1} \tag{11}$$

$$IC = \sum_{\boldsymbol{d}_{POI,j}} w_{POI,j} IC_{POI,j} \tag{12}$$

where the initial POI variance is modified with the new observations variances $\sigma(\boldsymbol{r}_i, \boldsymbol{d}_{POI,j})$ through the mixing function of Eq. (11). Afterwards, all the contributions of the POI are added considering specific weights for the POI according to their relative importance (Eq. (12)). Such a factor can be defined to drive the inspection towards specific features of the target body. The variance of a new observation of a POI from an observation point is then modelled as:

$$\sigma(\boldsymbol{r}_i, \boldsymbol{d}_{POI,j}) = \begin{cases} \|\boldsymbol{r}_i - \boldsymbol{d}_{POI,j}\|^2 & \text{if VIS and ILL} \\ \infty \end{cases} \tag{13}$$

where VIS, denotes that the POI is visible, whereas ILL denotes that the POI is illuminated in that portion of orbit. The variance will decrease as the square of the distance between the POI and the servicer decreases according to the behaviour of visual-based observations and image quality, provided visibility and illumination conditions are satisfied. The formulation of this metric aims to minimise the variances of individual POI through observations under good conditions. The mixing function of Eq. (11) combines all observations in a single trajectory to score the relative orbits and accounts for the diminishing value of performing observations of the same POIs multiple times. This will provide preference in the motion planning optimisation to trajectories which observe POIs with high variance, favouring exploration of unknown and poorly observed parts of the carrier.

### 5.2. Safe information cost motion planning

The algorithm used for the information cost-based motion planning for the nanosatellite to inspect the ION carrier is defined considering the optimisation of the information cost metric. A sequential greedy algorithm for the selection of the relative orbits based on the information cost is used as in the work of [17]. The sequential greedy approach performs a selection heuristic of the next-best-view relative trajectory

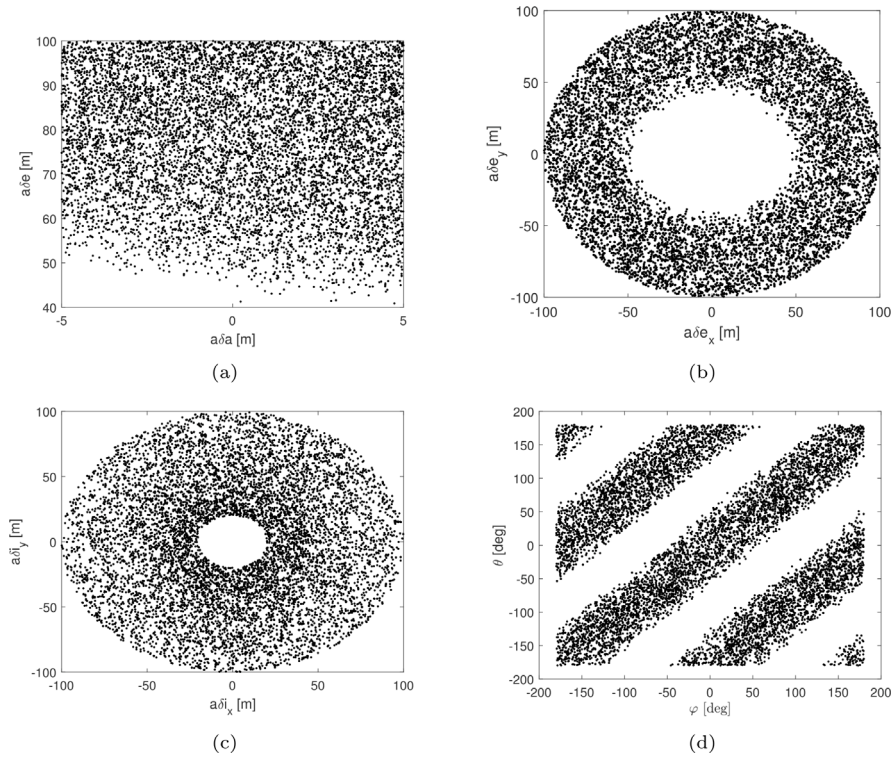


**Fig. 3.** ROE states space representation of passively safe relative trajectories. (a) representation in the $a\delta a/a\delta e$ space, (b) representation in the $a\delta e_x/a\delta e_y$ space, (c) representation in the $a\delta i_x/a\delta i_y$ space, (d) representation in the $\varphi/\theta$ space (phases of the relative eccentricity and inclination vectors respectively).

from a pre-loaded sampling of the relative trajectory space $\mathcal{S}(\delta\boldsymbol{\alpha})$. An additional feature of the approach of this paper is to introduce the initial sampling of trajectories constrained by the passive abort safety condition of Eq. (9). In particular, the passive abort safety check on the trajectory state is done considering the initial trajectory errors in terms of position and velocity ($\sigma_{t,r}$ and $\sigma_{t,v}$ respectively), and the differential drag perturbation quantities $a\dot{\delta\boldsymbol{\alpha}}$, see Section 3, together with their initial uncertainty $\sigma_{dd}$. Moreover, the time $\Delta T_{safe}$ necessary to ensure a secure passive trajectory abort is taken into account. For all instances of Gate II demonstrations within the SpEye mission, this $\Delta T_{safe}$ period is set equal to 12 h. Through these constraints, the initial safe set $\mathcal{S}_{safe}(\delta\boldsymbol{\alpha})$ is generated to be used in the sampling-based motion planning.

Jointly with the information cost metric, the safe set of trajectories generated is ranked considering also quantity which represents the transfer cost to move from the current relative orbits to the desired selected safe relative orbit. This will be combined with the information cost to compose the inspection cost $J_{insp}$ function, used to finally select the next relative orbit to implement. To retain the analytic evaluation of the inspection cost function with respect to the trajectories states, the transfer cost metric is defined as the quadratic form of the distance between the current and next ROE denoted as $\Delta\delta\boldsymbol{\alpha}$. This definition directly relates to the delta-v to be spent in the transfers between the two ROEs [51]. The inspection cost function can then be expressed as:

$$J_{insp} = IC + \Delta\delta\boldsymbol{\alpha}^T \mathrm{W}_{\delta v} \Delta\delta\boldsymbol{\alpha} \tag{14}$$

where $\mathrm{W}_{\delta v}$ is a parameter matrix, used to weight the transfer cost with respect to the information cost contributions in the motion planning optimisation. The matrix is defined considering that only diagonal terms can have values different from zero as follows:

$$\mathrm{W}_{\delta v} = w_{\delta v} \begin{bmatrix} w_{\delta a} & 0 & 0 & 0 & 0 & 0 \\ 0 & w_{\delta\lambda} & 0 & 0 & 0 & 0 \\ 0 & 0 & w_{\delta e_x} & 0 & 0 & 0 \\ 0 & 0 & 0 & w_{\delta e_y} & 0 & 0 \\ 0 & 0 & 0 & 0 & w_{\delta i_x} & 0 \\ 0 & 0 & 0 & 0 & 0 & w_{\delta i_y} \end{bmatrix} \tag{15}$$

where the weights $w_{(\cdot)}$ are scalar values.

Algorithm 1 details the motion planning logic based on the information cost formulated in this work.

**Algorithm 1:** Pseudo-code of the inspection trajectory planning

**Input:** $\delta\boldsymbol{\alpha}_{CPRO}$, $\Delta T_{insp}$, $\sigma_{t,r}$,$\sigma_{t,v}$, $a\dot{\delta\boldsymbol{\alpha}}$, $\sigma_{dd}$, $\Delta T_{safe}$, $C_{coll}$, $POI$, $\sigma_{POI,0}$, $\mathrm{MODE}_{transfer}$, $\mathrm{W}_{\delta v}$

Uniform sample the $\mathcal{S}(\delta\boldsymbol{\alpha})$ space
Generate $\mathcal{S}_{safe}(\delta\boldsymbol{\alpha})$ subspace by applying the passive abort safety conditions of Equation (9).
**while** *inspection not complete* **do**
  **for** $a\delta\boldsymbol{\alpha}_i \in \mathcal{S}_{safe}$ **do**
    Discretise the inspection trajectory $a\delta\boldsymbol{\alpha}_i$ over $\Delta T_{insp}$ time interval.
    Compute information cost from initial POI variance $\sigma_{POI,0}$ with Equations (11) and (12).
    Compute transfer cost metric analytically, $\Delta\delta\boldsymbol{\alpha}^T \mathrm{W}_{\delta v} \Delta\delta\boldsymbol{\alpha}$ depending on $\mathrm{MODE}_{transfer}$
  Apply sequential greedy heuristic to select next best inspection orbit $a\delta\alpha_{insp,i}$ according to Equation (14)
  Perform transfer $a\delta\alpha_{insp,i-1} \rightarrow a\delta\alpha_{insp,i}$
  Update POI variances $\sigma_{POI,0}$ with actual observations taken on $a\delta\alpha_{insp,i}$ for $\Delta T_{insp}$ with Equation (11)

The algorithm to compute the actual transfer trajectory and obtain the actual delta-v expenditure for the transfers will be detailed in Section 6.

### 5.3. Simulation results: demo 2.1

In this section the simulation results for the first demonstration of Gate II are presented, considering the application of the inspection motion planning algorithm described in Section 5.2. In this experiment the ION target attitude motion is stable in the orbital RTN frame, thus the POIs defined on the target's body are constant in the RTN over time.

Two separate scenarios are simulated considering the different fundamental shapes of the inspection trajectories contained in the safe state space $S_{safe}$:

- **Stable inspection orbits**: here bounded stable relative orbits with energy matching conditions $a\delta a = 0$ m are considered in the safe state space $S_{safe}$. The inspection time $\Delta T_{insp}$ used in these cases to evaluate the information cost is set equal to 1 orbital period.
- **Drifting inspection orbits**: here general drifting inspection orbits with $a\delta a \neq 0$ are selected in the safe state space $S_{safe}$. The inspection time $\Delta T_{insp}$ used in these cases is set equal to 5 orbital periods.

As far as the transfer modes $MODE_{transfer}$ between the inspection orbits designed $a\delta\boldsymbol{\alpha}_{insp,i}$, the strategy described hereafter is adopted. Between each inspection orbits, an intermediate parking orbit $CPRO_i$ is considered with energy matching condition $a\delta a = 0$ m, $a\delta\lambda = 300$ m, $\|\delta\boldsymbol{e}\| = 50$ m, $\|\delta\boldsymbol{i}\| = 50$ m, $\varphi_i = \varphi_{i-1}$, $\theta_i = \theta_{i-1}$. It is worth mentioning that the corresponding phase of the relative eccentricity and inclination vectors in the CRPO-i are intentionally kept identical to those of the preceding inspection orbits. This preservation guarantees a reduction in delta-v expenditure during the transfer. The peculiar strategy selected for the transfers between relative orbits considering intermediate parking relative orbits was implemented due to operational constraints of the mission, arising from power and data budget considerations. The transfers from the $i-1$th inspection orbits to the CRPO-i and from the CPRO-i to the $i$th inspection orbits are determined through the optimal control solution involving a fixed time of flight. The details of the latter strategy are provided in Section 6. All simulations are referred to the operational SSO orbit with LTAN 00:00 h. Given the small dimensions of the target with respect to the distances involved in the geometry of the relative orbits identified in the safe set, the following approximation has been introduced. In these simulations, the distance between the servicer and the target's POIs is treated as equal to the distance from the target's centre of mass, which serves as the origin of the RTN frame. This approach results in a POI definition where the relevant parameters are identified only in their normal direction to the surface on which they are located.

The parameters used in the demo 2.1 simulations are reported in Table 4. The quantities $\gamma_{vis}$ and $\gamma_{ill}$ represent respectively the maximum angles of viewing and illumination of a feature with respect to the servicer camera and sun direction. The $r_{max}$ value is the maximum distance where observations with the required resolution can be performed, set based on the camera specifications.

Fig. 4 shows the inspection trajectories designed with the inspection motion planning algorithm considering stable orbit set $S_{safe}$ case. Note that the sequence is stopped after four inspection orbits thanks to having reached a satisfactory inspection performance. In the depicted figure, the red markers represent locations on the relative orbit where the formation is during the eclipse, rendering the observations unavailable (recall ILL in Eq. (13)). On the other hand, the green markers show the observation points planned by the algorithm, which considers a maximum observation distance of 100 m coherently with the requirements posed by the visible camera embarked by the free-flyer. In Fig. 4 the map of the single POIs information cost is displayed on a representative sphere. Note that the sphere is not representative of the actual dimension of the carrier spacecraft. It can be observed how two unobserved spots appear, specifically in the positive and negative vertical direction of the orbit normal. This is related only to the fact that due to the LTAN value selected and the fixed motion in RTN of the POI, few of them are never illuminated within the $\gamma_{ill}$ threshold by the Sun.

**Table 4**
Parameters of the inspection motion planning algorithm used for demo 2.1 simulations.

| | Stable IO | Drifting IO |
|---|---|---|
| POI | 162 uniformly distr. on a sphere | same as Stable IO |
| $N_{sample}$ | 1000 | same as Stable IO |
| $\Delta T_{insp}$ | 1 period | 5 periods |
| $N_{insp}$ | 120 | 600 |
| $N_{orbits}$ | 4 | 3 |
| $r_{max}$ (VIS) | 100 m | same as Stable IO |
| $\gamma_{vis}$ (VIS) | 70 deg | same as Stable IO |
| $\gamma_{ill}$ (ILL) | 85 deg | same as Stable IO |
| $\sigma_{t,r}$ | 20 cm ($1\sigma$) | same as Stable IO |
| $\sigma_{t,v}$ | 5 mm/s ($1\sigma$) | same as Stable IO |
| $\Delta T_{safe}$ | 12 h | same as Stable IO |
| $C_{coll}$ | 4 m | same as Stable IO |
| $a\delta\boldsymbol{\alpha} = [a\delta a, a\delta e_x, a\delta e_y]$ | [−8.2e−5, 0 , 0] m/s | same as Stable IO |
| $\sigma_{dd}$ | [4.1e−5, 1e−8, 1e−8] m/s ($1\sigma$) | same as Stable IO |
| $\sigma_{POI,0}$ | 1e6 m$^2$ | same as Stable IO |
| $W_{\delta v}$ [–] | Table 5 | Table 6 |
| Transfer time | 2 periods | 4 periods |
| $U_{max}$ transfer | 5e−4 m/s$^2$ | same as Stable IO |

Fig. 5 shows the comparison for the same test case of Fig. 4 of the sequence design using the proposed sequential greedy algorithm against another more advanced optimisation method, namely the genetic algorithm. In the latter method, instead of performing the minimisation of the total information cost defined on the target POI by sequentially selecting the next-best trajectory to fly, the sequence is optimised altogether, considering the cumulative cost of all trajectories in a combined way. Here ideally the selection of the next-best trajectory that will result in a costly next iteration will be avoided by considering the cost together. Of course, the computational effort to solve the optimisation problem with the genetic algorithm heuristic is far greater than the sequential greedy approach. In the simulations of this paper, the genetic algorithm implemented in MATLAB is used considering a population size of 1000 and function tolerance of 1e−3 [52]. Fig. 5 shows that the results produced by the two algorithms are comparable in performance, demonstrating the feasibility of using a simple and more computationally efficient method to minimise such cost function. This aspect is particularly relevant for implementing the planning onboard the free flyer. For reference, the motion planning algorithm for the test case presented in Demo 2.1, depicted in Fig. 5, utilised the sequential greedy approach, requiring 5.3 s, whereas the genetic algorithm heuristic took 16.6 min. In the sequential greedy solution, the initial sampling of the ROE state space is not included in the computational time; it is a pre-computed set that can be obtained offline. The initial evaluation of the algorithms' performances was conducted using a MATLAB implementation running on a machine equipped with an Intel(R) Core(TM) i7-8700 @3.20 GHz processor and 16 GB of RAM.

Multiple simulations have been performed to study the impact of the weight of the transfer cost metric in the inspection cost function. Specifically, the value of $w_{\delta v}$ has been changed while maintaining all the diagonal values in the matrix of Eq. (15) equal to ones. Fig. 6 and Table 5 report the results of the stable orbits inspection design of demo 2.1 considering different weight values of the delta-v metric of Eq. (14) with respect to the information cost. As reported in the table, it can be noted how for the $w_{\delta v} = 50$ case the inspection maintains the same information cost performances but with lower delta-v. This demonstrates the effectiveness of including in the selection algorithm a quantity to weight the relative orbits with the transfer cost, which leads to finding trajectories with good information cost but less costly to implement. Furthermore, the results for the case of $w_{\delta v} = 500$ show that excessively increasing the delta-v weight leads to a further decrease of

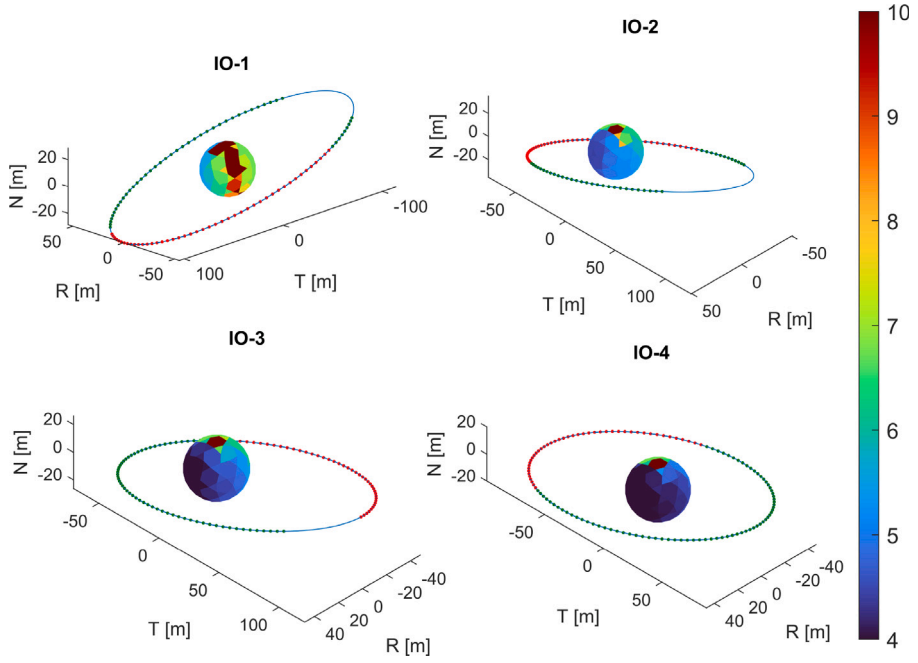


**Fig. 4.** Trajectories of the four **stable** inspection orbits computed with the sequential greedy sampling algorithm considering the information cost only ($w_{\delta v} = 0$) in the inspection cost of Eq. (14). The colorbar represents the logarithm of the information cost of each of the defined POIs on ION and stable in RTN. (For interpretation of the references to colour in this figure legend, the reader is referred to the web version of this article.)

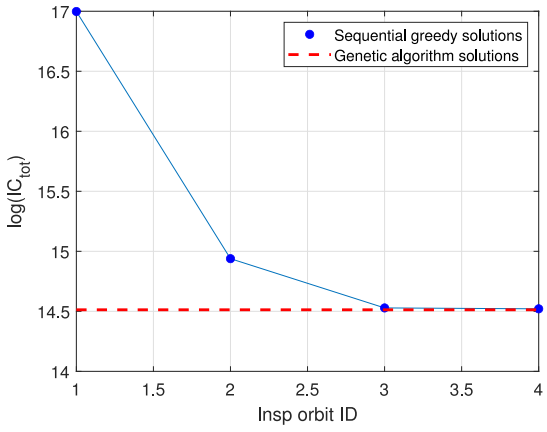


**Fig. 5.** Total inspection cost along the sequence of the sequential greedy solution (blue), against the one obtained with the genetic algorithm approach (red). (For interpretation of the references to colour in this figure legend, the reader is referred to the web version of this article.)

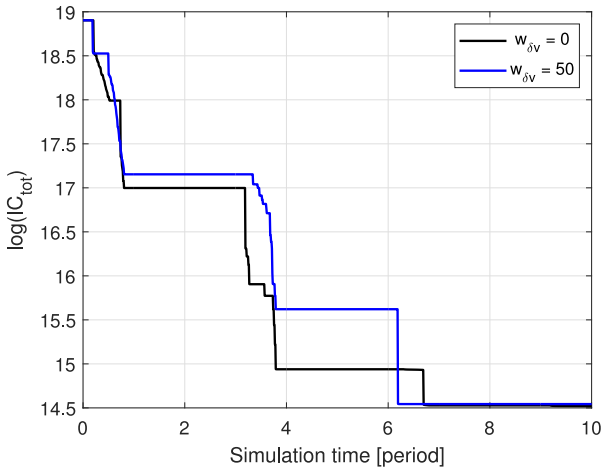


**Fig. 6.** Time evolution of the total information cost computed over the POI considered in the case with $w_{\delta v} = 0$ and $w_{\delta v} = 50$ for stable inspection orbits in Demo 3.1. Note that the hold-time spent in the intermediate parking orbits CPRO is not considered. Here just the transfer time is considered in the plot.

**Table 5**
Simulation results for different weight of the delta-v cost contribution $w_{\delta v}$ for the **stable** inspection orbits.

| | $\delta v_{tot}$ [m/s] | $log(IC_{tot})$ [–] |
|---|---|---|
| $w_{\delta v} = 0$ | 0.660 | 14.52 |
| $w_{\delta v} = 50$ | 0.510 | 14.53 |
| $w_{\delta v} = 500$ | 0.480 | 15.54 |

the delta-v spent in the transfer but at the expense of the inspection effectiveness (minimisation of total information cost $IC_{tot}$).

Fig. 7 shows the results obtained considering the drifting relative orbit in the safe state space $S_{safe}$. Specifically, in this case, the sequence uses three successive drifting orbits which last five orbital periods each. This is set taking into account the satisfactory inspection performances (in terms of minimisation of the information cost) are reached after three relative inspection orbits. It is worth noticing that with respect to the stable orbit conditions, here the drifting motion and the longer time of inspection allow sufficient exploration of observation points in fewer orbits to reach satisfactory inspection performances. Table 6 shows the results of the inspection motion planning algorithm for drifting inspection orbits varying the delta-v weight in Eq. (14).

## 6. Gate III: Close-range rendezvous

In Gate III the objective of the SpEye mission is to demonstrate safe and autonomous close-range rendezvous capabilities of a nanosatellite in proximity of an object in LEO. The in-orbit demonstrations, outlined in Section 2 and Table 2, are designed to showcase capabilities applicable to different servicing/removal scenarios. The present section details the guidance strategy envisioned for the SpEye rendezvous demonstrations.

**Table 6**
Simulation results for different weight of the delta-v cost contribution $w_{\delta v}$ for the **drifting** inspection orbits.

| | $\delta v_{tot}$ [m/s] | $log(IC_{tot})$ [–] |
|---|---|---|
| $w_{\delta v} = 0$ | 0.511 | 14.51 |
| $w_{\delta v} = 50$ | 0.391 | 14.52 |
| $w_{\delta v} = 500$ | 0.448 | 14.52 |
| $w_{\delta v} = 1000$ | 0.346 | 14.52 |
| $w_{\delta v} = 2000$ | 0.313 | 15.90 |

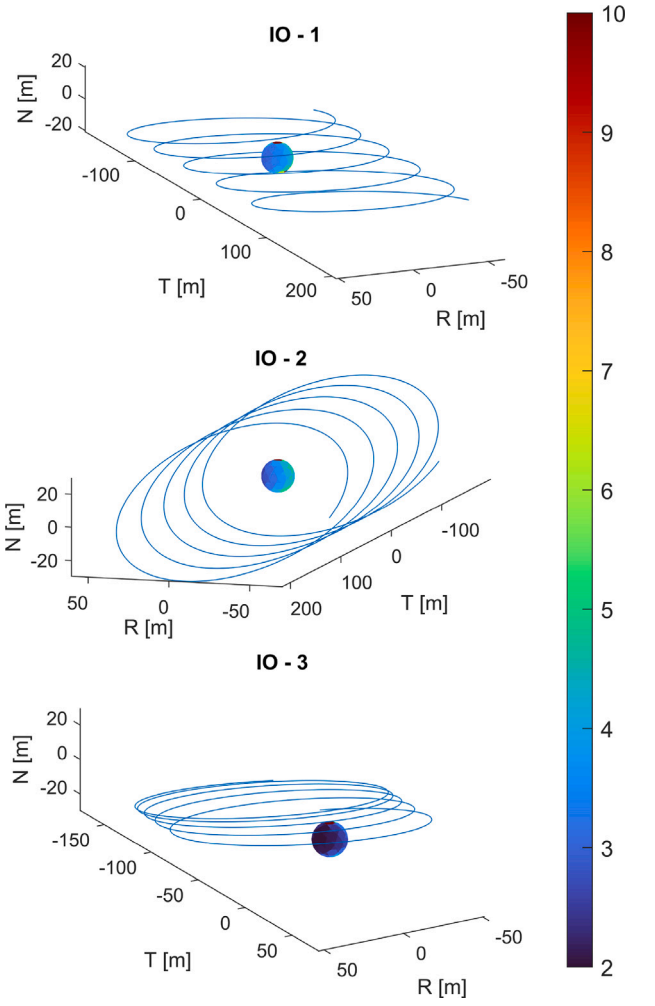


**Fig. 7.** Trajectories of the three **drifting** inspection orbits computed with the sequential greedy sampling algorithm considering the information cost only ($w_{\delta v} = 0$ in the inspection cost of Eq. (14). The colorbar represents the logarithm of the information cost of each of the defined POI defined on ION and stable in RTN. (For interpretation of the references to colour in this figure legend, the reader is referred to the web version of this article.)

The close range rendezvous guidance problem, at this project development phase, is formulated as a 3 DOF optimal control problem with fixed time-of-flight. Specifically, the fixed time of flight is limited to the time interval that the formation remains outside the eclipse condition and it is set to half orbital period. This necessity arises from the requirement for the visual relative navigation suite to guarantee a reliable solution during the approach. The guidance scheme is based on the work of Borelli et al. [31], where the fixed-time fuel-optimal control problem of forced-motion proximity flight is solved considering novel safety path constraints. Particularly, the following safety levels are modelled in the scheme:

- *Passive Abort Safety (PAS) constraints*: at each applied node, the ROE state is constrained to respect a minimum one-orbit distance in the RN plane considering generic ROE conditions, e.g. non-parallel relative eccentricity and relative inclination vector and non-null relative semi-major axis. This guarantees, in the Keplerian relative orbits assumption, collision avoidance of the uncontrolled trajectory after a failure without the application of any collision avoidance policy.
- *Active Collision Safety (ACS) constraints*: at each applied node, the trajectory is constrained to guarantee a minimum one-orbit distance in the RT plane after a failure with the application of a collision avoidance policy.

More details on the formulation of the safety constraints can be found in Borelli et al. [31].

After the transcription of the problem in $N$ time nodes between initial time $t_0$ and the final time $t_f$ the optimal control problem is expressed as:

$$\min_{\mathbf{f}_{c,i},\mathbf{f}^{ACS}_{cm,j}} \quad \sum_{i=1}^{N} \|\mathbf{f}_{c,i}\|_1 + \lambda_{ACS} \sum_{m}^{M} \sum_{j=1}^{J} \|\mathbf{f}^{ACS}_{cm,j}\|_1 \tag{16a}$$

$$\text{s.t.} \quad \delta\boldsymbol{\alpha}_f = \boldsymbol{\Phi}_{0,i}\delta\boldsymbol{\alpha}_0 + \mathrm{H}_f U \tag{16b}$$

$$\delta\boldsymbol{\alpha}(t_0) = \delta\boldsymbol{\alpha}_0 \tag{16c}$$

$$\mathcal{P}_{PAS}(\delta\boldsymbol{\alpha}_i, R_{KOZ,RN}) < 0 \tag{16d}$$

$$\mathcal{P}_{ACS}(\delta\boldsymbol{\alpha}_i, R_{KOZ,RT}) < 0 \tag{16e}$$

$$\mathcal{P}_{ACS}(\delta\boldsymbol{\alpha}_i) = 0 \tag{16f}$$

$$\|\mathbf{u}_i\|_\infty < U_{max} \tag{16g}$$

$$\|\mathbf{u}^{ACS}_{m,j}\|_\infty < U^{ACS}_{max} \tag{16h}$$

where the functions $\mathcal{P}(\cdot)$ represent the PAS and ACS inequality and equality constraints at the applicable nodes, while $R_{KOZ,RN}$ and $R_{KOZ,RT}$ the KOZ radius in the RN and RT plane respectively. The nominal control accelerations $\mathbf{f}_c$ and collision avoidance policy accelerations $\mathbf{f}^{ACS}_c$ are considered in the cost functions with the 1-norm formulation, while their $\infty$-norm is constrained by the maximum acceleration levels. The ACS collision avoidance policy is included in the cost function weighted by the vector $\lambda_{ACS}$. This strategy is developed to guarantee the finding solutions that do not require excessive amount of fuel in the escape manoeuvres in case of an abort, together with the fuel-efficiency of the nominal trajectory. The Non Linear Programming (NLP) problem is solved with a Sequential Convex Programming (SCP) method in order to properly handle the non-convexity introduced in the optimisation problem by the safety constraints of Eqs. (16d)–(16f). More details on the SCP algorithm and safety constraints formulations can be found at the reference Borelli et al. [31]. The described safety enhanced guidance algorithm is used to preliminary design the autonomous close range demonstrations for the SpEye mission shown in Table in 2.

### 6.1. Demo 3.1

In the first demonstration of autonomous close-range rendezvous, the chaser starts from the parking orbit 1, characterised by a ROE equal to $a\delta\boldsymbol{\alpha} = [0, 50, 50, 0, 50, 0]$ m. The selection of parking orbit 1 as initial condition for the close-range rendezvous with respect to the CRPO was driven by the time-of-flight constraints of half an orbital period induced by the eclipse conditions. Specifically, a closer starting relative parking orbit enables a slower rendezvous, which makes less critical meeting the safety constraints along the trajectory. In this demonstration, the approach is performed towards a stable hold point in the target centred RTN frame at a 10 m distance in the +T direction. The KOZ around the target for the safety constraints is considered with a 8 m radius. The rendezvous demonstration is subdivided in the following sub-phases:

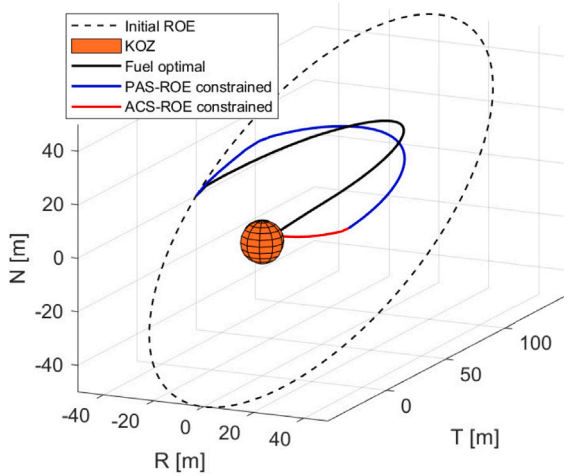


**Fig. 8.** Trajectories in the RTN of the fuel optimal (black) and safe guidance scheme (blue+red) for the demo 3.1 of the SpEye mission. (For interpretation of the references to colour in this figure legend, the reader is referred to the web version of this article.)

**Table 7**
Delta-v consumption of the fuel optimal and safe guidance scheme considered for demo 3.1.

| | |
|---|---|
| Fuel optimal | 0.161 m/s |
| Safe guidance | 0.168 m/s |

- Forward rendezvous to the stable hold point at 10 m.
- Hold point station keeping for $\Delta T_{sk}$ in the RTN frame.
- Backward transfer to the CRPO parking orbit.

In this paper, the simulation results of the forward rendezvous approach are presented to showcase the effectiveness and peculiarity of the strategy. Fig. 8 displays the trajectories obtained with both the safe guidance scheme and the fuel-optimal only case in the target-centred RTN frame. Indeed one can observe how the nominal trajectories show a different behaviour, mainly driven by the safety constraints introduced in the optimisation procedure. In the safe guidance scheme, the first 75% of the trajectory is constrained with PAS, while the last segment is constrained with ACS conditions. Fig. 9 shows the projection of the ROE relative orbits propagations related to the PAS constrained nodes for the fuel optimal case and safety constrained case of demo 3.1. It is clear how in the safe guidance scheme case with PAS applied, the minimum RN one-orbit separation is guaranteed in the first 75% of the trajectory while is not in the fuel-optimal only case. Note that this passive abort safety result is obtained in conditions different than the conventional E/I separation phasing. The delta-v cost of the fuel optimal scheme and safe guidance scheme are reported in Table 7, demonstrating how the improvement in flight safety of the close-range rendezvous trajectory can be achieved with only a small increase in the nominal delta-v spent along the nominal trajectory.

### 6.2. Demo 3.3

In demo 3.3 the SpEye mission aims to demonstrate the free-flyer capability of performing a rendezvous to a hold point near the target with a more complex motion. Specifically, an approach to a rotating hold point in RTN with a circular motion around ION at 10 m distance and at a 1 deg/s angular rate is planned. The objective of this demonstration scenario is to depict synchronisation to the rotational movement of an uncontrolled object in space, as typically occur when a debris is captured by means of a robotic arm. This condition will result in the creation of rendezvous trajectories, which typically demand higher control effort, making them more energetically intensive. As a result, these trajectories will pose greater challenges from a safety perspective.

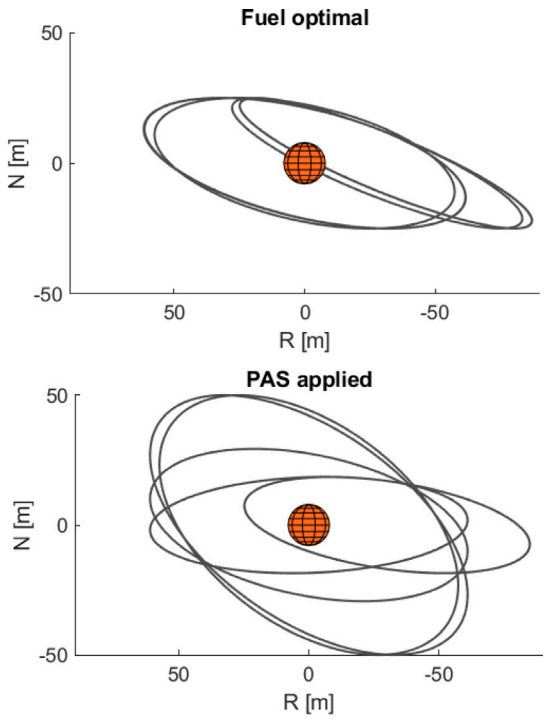


**Fig. 9.** Projection of the relative trajectory of demo 3.1 in the RN plane related to the ROE states of PAS constrained nominal nodes for the fuel optimal solution (top), and safe guidance solution (bottom).

**Table 8**
Delta-v consumption of the fuel optimal and safe guidance scheme considered for demo 3.1.

| | |
|---|---|
| Fuel optimal | 0.298 m/s |
| Safe guidance | 0.315 m/s |

The demonstration operations are analogous of the one for demo 3.1 listed in Section 6.1, with the only difference of the hold point final condition and of the reduced station keeping time in the hold point at 10 s. As for demo 3.1, the forward rendezvous trajectory is still required to be completed in half a period to guarantee that the whole transfer trajectory which exploits visual based navigation remains outside the eclipse condition.

In Fig. 10 the forward rendezvous trajectories for the safe guidance scheme and the fuel optimal scheme are shown, where again the first 75% of the transfer is constrained by PAS, while in the last section ACS constraints are applied. Again, as displayed in Fig. 11, the safe guidance algorithm is capable of capturing a safer trajectory which guarantees RN minimum one-orbit separation of the PAS constrained nodes. Table 8 shows the delta-v consumption of the fuel optimal and safe guidance solution, which demonstrate the higher delta-v consumption with respect to the stable condition while ensuring a small incremental cost of the safe guidance scheme with respect to the fuel optimal scheme also for the test case of demo 3.3.

## 7. Conclusion

This paper outlines the mission design, as well as the guidance and control strategies of the SpEye CubeSat mission, which is a part of the Alcor program under Agenzia Spaziale Italiana (ASI). The objective of the mission is to demonstrate the proximity operations capabilities necessary for servicing and ADR missions envisioned in future sustainable space infrastructure. For this purpose, a 6U CubeSat is a useful and cost-effective test bed for these demonstrations, as well as for potential future deployment in proximity operations missions, such as for

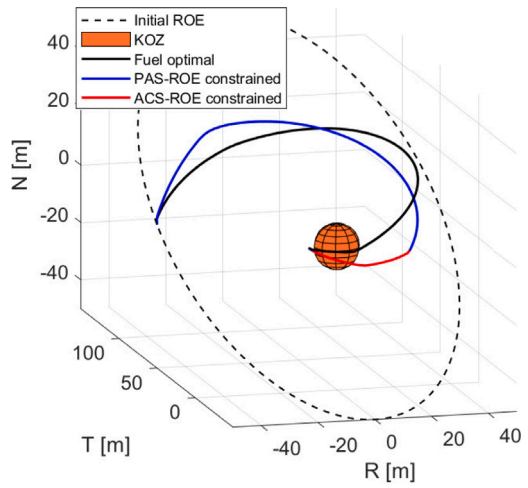


**Fig. 10.** Trajectories in the RTN of the fuel optimal (black) and safe guidance scheme (blue+red) for the demo 3.3 of the SpEye mission. (For interpretation of the references to colour in this figure legend, the reader is referred to the web version of this article.)

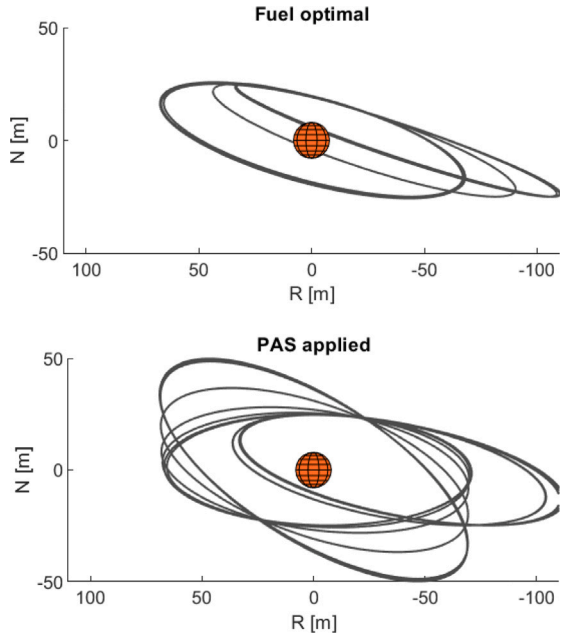


**Fig. 11.** Projection of the relative trajectory of demo 3.3 in the RN plane related to the ROE states of PAS constrained nominal nodes for the fuel optimal solution (top), and safe guidance solution (bottom).

inspection and secondary tasks. The paper details the developments undertaken during phase 0/A of the project, focusing on the difficulties of proximity operations with a nanosatellite to another object in low Earth orbit. The planned operations and demonstrations of the nanosatellite released by its carrier are presented, showing the peculiarities and their applicability in servicing and removal scenarios. The mission design presented highlights the flight safety feature of proximity operations, which enables the success, efficiency and robustness of proximity flight especially with a low-cost and limited capability nanosatellite platform. The safety peculiarities of the design have been highlighted, focusing on the description of the inspection motion planning and the forced motion rendezvous methods. In the inspection and approach demonstration planned, the concept of passive abort safety was extensively applied to guarantee collision avoidance without the need of an active collision policy and lower the ground support required in operations. An efficient sampling-based algorithm is presented which is capable of achieving optimal exploration of the target's features with relative inspection orbits which are characterised by a high level of passive abort safety. Moreover, the application of a safe guidance scheme to forced motion rendezvous trajectories demonstrated the capability of improving the safety and robustness of the delicate close-range trajectories, without impacting the nominal cost of the manoeuvres. These strategies are devised to effectively meet the stringent trajectory safety requirements specific to the SpEye CubeSat mission. Future developments planned in phase B of the project will tackle the integration of the guidance and control strategies with the navigation modes in each demonstration. Moreover, the assessment of the strategies presented will be evaluated with Monte Carlo simulations.

## Declaration of competing interest

The authors declare that they have no known competing financial interests or personal relationships that could have appeared to influence the work reported in this paper.

## Acknowledgements

This work is supported by the Italian Space Agency under the ALCOR programme, contract ASI n. 2023-1-I.0 "Space Eye - SpEye". The Authors would like to acknowledge all the SpEye consortium members for their contribution to the project

## References

[1] T. Mulder, Orbital express autonomous rendezvous and capture flight operations, Part 2 of 2: AR&C exercise 4, 5, and end-of-life. arXiv:https://arc.aiaa.org/doi/pdf/10.2514/6.2008-6768, http://dx.doi.org/10.2514/6.2008-6768, URL https://arc.aiaa.org/doi/abs/10.2514/6.2008-6768.

[2] I. Kawano, M. Mokuno, T. Kasai, T. Suzuki, Result of autonomous rendezvous docking experiment of engineering test satellite-VII, J. Spacecr. Rockets 38 (1) (2001) 105–111, http://dx.doi.org/10.2514/2.3661, arXiv:https://doi.org/10.2514/2.3661.

[3] M. Vavrina, C. Skelton, K. Deweese, B. Naasz, D. Gaylor, C. D'souza, Safe rendezvous trajectory design for the restore-l mission, in: Advances in the Astronautical Sciences, 2019, pp. 3649–3668.

[4] R. Biesbroek, S. Aziz, A. Wolahan, S.-f. Cipolla, M. Richard-Noca, L. Piguet, The clearspace-1 mission: Esa and clearspace team up to remove debris, in: Proc. 8th European Conference on Space Debris, 2021, pp. 1–3.

[5] T. Yamamoto, J. Matsumoto, H. Okamoto, R. Yoshida, C. Hoshino, K. Yamanaka, Pave the way for active debris removal realization: JAXA commercial removal of debris demonstration (CDR2), in: Proc. 8th European Conference on Space Debris, 2021.

[6] J.L. Forshaw, G.S. Aglietti, S. Fellowes, T. Salmon, I. Retat, A. Hall, T. Chabot, A. Pisseloup, D. Tye, C. Bernal, F. Chaumette, A. Pollini, W.H. Steyn, The active space debris removal mission RemoveDebris. Part 1: From concept to launch, Acta Astronaut. 168 (2020) 293–309, http://dx.doi.org/10.1016/j.actaastro.2019.09.002, URL http://www.sciencedirect.com/science/article/pii/S0094576519312512.

[7] J. Forshaw, R. Lopez, A. Okamoto, C. Blackerby, N. Okada, The ELSA-d end-of-life debris removal mission: Mission design, in-flight safety, and preparations for launch, in: Proceedings of the Advanced Maui Optical and Space Surveillance Technologies Conference, 17-20 September, 2019, Maui, Hawaii, 2019, pp. 44–50.

[8] C.W. Roscoe, J.J. Westphal, E. Mosleh, Overview and GNC design of the CubeSat proximity operations demonstration (CPOD) mission, Acta Astronaut. 153 (2018) 410–421, http://dx.doi.org/10.1016/j.actaastro.2018.03.033, URL https://www.sciencedirect.com/science/article/pii/S0094576517314042.

[9] S.M. Pedrotty, J.J. Sullivan, E.A. Gambone, Thomas, Kirven, Seeker free-flying inspector gnc system overview, 2019.

[10] E.C. Team, e.Inspector CDF Study Report - Assessment of an ENVISAT Imaging Mission as a Precursor to a Potential ENVISAT Deorbit, Tech. rep., European Space Agency (ESA), 2017.

[11] S. Silvestrini, J. Prinetto, G. Zanotti, M. Lavagna, Design of robust passively safe relative trajectories for uncooperative debris imaging in preparation to removal, 175 4205–4222, URL https://www.scopus.com/inward/record.uri?eid=2-s2.0-85126240899&partnerID=40&md5=6a51911e8e10ed060ac72ea48b7bbcb5.

[12] O. Montenbruck, M. Kirschner, S. D'Amico, S. Bettadpur, E/I-vector separation for safe switching of the GRACE formation, Aerosp. Sci. Technol. 10 (7) (2006) 628–635, http://dx.doi.org/10.1016/j.ast.2006.04.001, URL https://www.sciencedirect.com/science/article/pii/S1270963806000472.

[13] G. Borelli, G. Gaias, C. Colombo, Rendezvous and proximity operations design of an active debris removal service to a large constellation fleet, Acta Astronaut. 205 (2023) 33–46, http://dx.doi.org/10.1016/j.actaastro.2023.01.021, URL https://www.sciencedirect.com/science/article/pii/S0094576523000243.

[14] F. Capolupo, P. Labourdette, Receding-horizon trajectory planning algorithm for passively safe on-orbit inspection missions, J. Guid. Control Dyn. 42 (5) (2019) 1023–1032, http://dx.doi.org/10.2514/1.G003736, arXiv:https://doi.org/10.2514/1.G003736.

[15] M. Maestrini, P. Di Lizia, Guidance strategy for autonomous inspection of unknown non-cooperative resident space objects, J. Guid. Control Dyn. 45 (6) (2022) 1126–1136, http://dx.doi.org/10.2514/1.G006126, arXiv:https://doi.org/10.2514/1.G006126.

[16] A. Brandonisio, M. Lavagna, D. Guzzetti, Reinforcement learning for uncooperative space objects smart imaging path-planning, J. Astronaut. Sci. 68 (4) (2021) 1145–1169, http://dx.doi.org/10.1007/s40295-021-00288-7.

[17] Y.K. Nakka, W. Hönig, C. Choi, A. Harvard, A. Rahmani, S.-J. Chung, Information-based guidance and control architecture for multi-spacecraft on-orbit inspection, J. Guid. Control Dyn. 45 (7) (2022) 1184–1201, http://dx.doi.org/10.2514/1.G006278, arXiv:https://doi.org/10.2514/1.G006278.

[18] L. Breger, J.P. How, Safe trajectories for autonomous rendezvous of spacecraft, J. Guid. Control Dyn. 31 (5) (2008) 1478–1489, http://dx.doi.org/10.2514/1.29590.

[19] G. Gaias, M. Lovera, Safe Trajectory Design for Close Proximity Operations, Adv. Astronaut. Sci. 175 (2021).

[20] J. Ventura, M. Ciarcià, M. Romano, U. Walter, Fast and near-optimal guidance for docking to uncontrolled spacecraft, J. Guid. Control Dyn. 40 (12) (2017) 3138–3154.

[21] G. Boyarko, O. Yakimenko, M. Romano, Optimal rendezvous trajectories of a controlled spacecraft and a tumbling object, J. Guid. Control Dyn. 34 (4) (2011) 1239–1252, http://dx.doi.org/10.2514/1.47645, arXiv:https://doi.org/10.2514/1.47645.

[22] M. Leomanni, R. Quartullo, G. Bianchini, A. Garulli, A. Giannitrapani, Variable-horizon guidance for autonomous rendezvous and docking to a tumbling target, J. Guid. Control Dyn. 45 (5) (2022) 846–858, http://dx.doi.org/10.2514/1.G006340, arXiv:https://doi.org/10.2514/1.G006340.

[23] L. Palacios, M. Ceriotti, G. Radice, Close proximity formation flying via linear quadratic tracking controller and artificial potential function, Adv. Space Res. 56 (10) (2015) 2167–2176.

[24] I. Lopez, C.R. Mclnnes, Autonomous rendezvous using artificial potential function guidance, J. Guid. Control Dyn. 18 (2) (1995) 237–241, http://dx.doi.org/10.2514/3.21375, arXiv:https://doi.org/10.2514/3.21375.

[25] J.A. Starek, E. Schmerling, G.D. Maher, B.W. Barbee, M. Pavone, Fast, safe, propellant-efficient spacecraft motion planning under Clohessy–Wiltshire–Hill dynamics, J. Guid. Control Dyn. 40 (2) (2017) 418–438, http://dx.doi.org/10.2514/1.G001913, arXiv:https://doi.org/10.2514/1.G001913.

[26] H.B. Hablani, M.L. Tapper, D.J. Dana-Bashian, Guidance and relative navigation for autonomous rendezvous in a circular orbit, J. Guid. Control Dyn. 25 (3) (2002) 553–562, http://dx.doi.org/10.2514/2.4916, arXiv:https://doi.org/10.2514/2.4916.

[27] G. Gaias, S. D'Amico, Impulsive maneuvers for formation reconfiguration using relative orbital elements, J. Guid. Control Dyn. 38 (6) (2015) 1036–1049, http://dx.doi.org/10.2514/1.G000189.

[28] D. Morgan, S.-J. Chung, F.Y. Hadaegh, Model predictive control of swarms of spacecraft using sequential convex programming, J. Guid. Control Dyn. 37 (6) (2014) 1725–1740, http://dx.doi.org/10.2514/1.G000218, arXiv:https://doi.org/10.2514/1.G000218.

[29] P. Lu, X. Liu, Autonomous trajectory planning for rendezvous and proximity operations by conic optimization, J. Guid. Control Dyn. 36 (2) (2013) 375–389, http://dx.doi.org/10.2514/1.58436, arXiv:https://doi.org/10.2514/1.58436.

[30] N. Ortolano, D.K. Geller, A. Avery, Autonomous optimal trajectory planning for orbital rendezvous, satellite inspection, and final approach based on convex optimization, J. Astronaut. Sci. 68 (2) (2021) 444–479.

[31] G. Borelli, G. Gaias, C. Colombo, Safety in forced motion guidance for proximity operations based on relative orbital elements, in: AAS/AIAA 33rd Space Flight Mechanics Meeting, Austin, TX, 2023.

[32] D-orbit website, 2023, https://www.dorbit.space/, Accessed: 2023-08-31.

[33] V. Capuano, GNSS-Based Navigation for Lunar Missions (Ph.D. thesis), École Polytechnique Fédérale de Lausanne, 2016.

[34] V. Capuano, G. Cuciniello, V. Pesce, R. Opromolla, S. Sarno, M. Lavagna, M. Grassi, F. Corraro, G. Capuano, P. Tabacco, F. Meta, M. Battagliere, A. Tuozzi, VINAG: A highly integrated system for autonomous on-board absolute and relative spacecraft navigation, in: 4S Symposium, 2018.

[35] R. Opromolla, A. Nocerino, G. Napolano, G. Fasano, M. Grassi, V. Capuano, S. Illiano, R. Votta, M. Rinaldi, G. Leccese, S. Natalucci, Electro-optical based relative navigation for close-range inspection and rendezvous in the SpEye CubeSat-based mission, in: AIAA SCITECH 2024 Forum, http://dx.doi.org/10.2514/6.2024-2453, arXiv:https://arc.aiaa.org/doi/pdf/10.2514/6.2024-2453, URL https://arc.aiaa.org/doi/abs/10.2514/6.2024-2453.

[36] V. Capuano, K. Kim, A. Harvard, S.-J. Chung, Monocular-based pose determination of uncooperative space objects, Acta Astronaut. 166 (2020) 493–506.

[37] V. Capuano, A. Harvard, Y. Lin, S.-J. Chung, DGNSS-vision integration for robust and accurate relative spacecraft navigation, in: Proceedings of the 32nd International Technical Meeting of the Satellite Division of the Institute of Navigation (ION GNSS+ 2019), 2019, pp. 2923–2939.

[38] V. Capuano, A. Harvard, S.-J. Chung, On-board cooperative spacecraft relative navigation fusing GNSS with vision, Prog. Aerosp. Sci. 128 (2022) 100761, http://dx.doi.org/10.1016/j.paerosci.2021.100761, URL https://www.sciencedirect.com/science/article/pii/S0376042121000646.

[39] IADC, Space Debris Mitigation Guidelines, Tech. rep., IADC Steering Group and Working Group 4, 2021.

[40] M. Wermuth, G. Gaias, S. D'Amico, Safe picosatellite release from a small satellite carrier, J. Spacecr. Rockets 52 (5) (2015) 1338–1347, http://dx.doi.org/10.2514/1.A33036, arXiv:https://doi.org/10.2514/1.A33036.

[41] G. Gaias, J.-S. Ardaens, Flight demonstration of autonomous noncooperative rendezvous in low earth orbit, J. Guid. Control Dyn. 41 (6) (2018) 1337–1354, http://dx.doi.org/10.2514/1.G003239, arXiv:https://doi.org/10.2514/1.G003239.

[42] S. D'Amico, Relative Orbital Elements as Integration Constants of Hill's Equations, Tech. rep., Deutsches Zentrum fr Luft- und Raumfahrt, Oberpfaffenhofen, Dec. 2005.

[43] G. Gaias, M. Lovera, Trajectory design for proximity operations: The relative orbital elements' perspective, J. Guid. Control Dyn. 44 (12) (2021) 2294–2302, http://dx.doi.org/10.2514/1.G006175, arXiv:https://doi.org/10.2514/1.G006175.

[44] G. Gaias, J.-S. Ardaens, O. Montenbruck, Model of $$j_2$$perturbed satellite relative motion with time-varying differential drag, Celestial Mech. Dynam. Astronom. 123 (4) (2015) 411–433, http://dx.doi.org/10.1007/s10569-015-9643-2.

[45] A.W. Koenig, T. Guffanti, S. D'Amico, New state transition matrices for spacecraft relative motion in perturbed orbits, J. Guid. Control Dyn. 40 (7) (2017) 1749–1768, http://dx.doi.org/10.2514/1.G002409, arXiv:https://doi.org/10.2514/1.G002409.

[46] J. Picone, A. Hedin, D.P. Drob, A. Aikin, NRLMSISE-00 empirical model of the atmosphere: Statistical comparisons and scientific issues, J. Geophys. Res. Space Phys. 107 (A12) (2002) SIA–15.

[47] S. D'Amico, O. Montenbruck, Proximity operations of formation-flying spacecraft using an eccentricity/inclination vector separation, J. Guid. Control Dyn. 29 (3) (2006) 554–563, http://dx.doi.org/10.2514/1.15114, arXiv:https://doi.org/10.2514/1.15114.

[48] E. Gill, S. D'Amico, O. Montenbruck, Autonomous formation flying for the PRISMA mission, J. Spacecr. Rockets 44 (3) (2007) 671–681, http://dx.doi.org/10.2514/1.23015, arXiv:https://doi.org/10.2514/1.23015.

[49] G. Gaias, J.-S. Ardaens, Design challenges and safety concept for the AVANTI experiment, Acta Astronaut. 123 (2016) 409–419, http://dx.doi.org/10.1016/j.actaastro.2015.12.034, Special Section: Selected Papers from the International Workshop on Satellite Constellations and Formation Flying 2015. URL https://www.sciencedirect.com/science/article/pii/S0094576515004737.

[50] M. Schwager, D. Rus, J.-J. Slotine, Unifying geometric, probabilistic, and potential field approaches to multi-robot deployment, Int. J. Robot. Res. 30 (3) (2011) 371–383, http://dx.doi.org/10.1177/0278364910383444, arXiv:https://doi.org/10.1177/0278364910383444.

[51] G. Gaias, S. D'Amico, J.-S. Ardaens, Generalised multi-impulsive manoeuvres for optimum spacecraft rendezvous in near-circular orbit, Int. J. Space Sci. Eng. 3 (1) (2015) 68–88.

[52] D.E. Goldberg, Genetic Algorithms in Search, Optimization, and Machine Learning, Addison-Wesley, New York, 1989.